Band structure and effective properties of one-dimensional thermoacoustic Bloch waves

Haitian Hao [*] and Fabio Semperlotti[†]

School of Mechanical Engineering, Purdue University, West Lafayette, Indiana 47907, USA

We investigate the dispersion characteristics and the effective properties of acoustic waves propagating in a one-dimensional duct equipped with periodic thermoacoustic coupling elements. Each coupling element consists of a classical thermoacoustic regenerator subject to a static spatial temperature gradient. When acoustic waves pass through the regenerator, thermal-to-acoustic energy conversion takes place and can either amplify or attenuate the wave, depending on the direction of propagation of the wave. The presence of the spatial gradient naturally induces a loss of reciprocity. This paper provides a comprehensive theoretical model as well as an in-depth numerical analysis of the band structure and of the propagation properties of this thermoacoustically coupled, tunable, one-dimensional metamaterial. Among the most significant findings, it is shown that the acoustic metamaterial is capable of supporting nonreciprocal thermoacoustic Bloch waves that are associated with a particular form of unidirectional energy transport. The nonreciprocal nature of the waveguide in the long wavelength limit is well understood by seeing the waveguide as an acoustic Willis material. The homogenized material properties following the Willis approach help both the analysis and the interpretation of the waveguide dynamic behavior in selected frequency ranges. Remarkably, the thermoacoustic coupling also allows achieving a zero refractive index that ultimately leads to phase-invariant propagating sound waves. This zero-index property is shown to have very interesting implications to attain acoustic cloaking.

I. INTRODUCTION

In recent years, the study of acoustic metamaterials has focused on the possibility of breaking reciprocity and on the resulting effects on the dispersion and propagation of sound [1–6]. In conventional acoustic waveguides (e.g., a hollow duct), sound waves are reciprocally transmitted between two points of the domain. Exciting the domain at a source *A* and measuring its response at a point *B* would yield the exact same response than if the source and the observation point were switched. However, this reciprocal wave transmission mechanism might not always be a desired feature. There are certain applications such as medical imaging [7] or telecommunications devices [8] whose performance can be significantly improved in the presence of unidirectional sound transmission. For completeness, it is worth mentioning that unidirectional propagation has been observed and studied either in nonreciprocal or topological systems. While, under certain conditions, the effect of the two systems on the wave propagation characteristics might be conflated, the two systems lead to unidirectional propagation by means of very different mechanisms. Indeed, many topologically nontrivial systems are still reciprocal in nature [9–12]. Focusing on nonreciprocity, nonreciprocal waves have been achieved in a variety of systems that leveraged, as an example, rotating fluids [1], active materials with spatiotemporal modulation [2,3], near-zero refractive index materials [13], and materials with strong nonlinearities [4–6]. Nonreciprocal propagation was also observed in thermoacoustically coupled systems consisting of torus-shaped thermoacoustic (TA) engines [14–17]. It was this class of systems that later inspired the design of TA diodes [18] and TA amplifiers [19]. Despite the long and distinguished history of the TA science and the more recent analysis of diodes and amplifiers, the systematic analysis and in-depth understanding of the dispersion and propagation properties in periodic TA waveguides have never been undertaken.

The current paper specifically addresses this latter point by presenting a comprehensive theoretical and numerical analysis of the dispersion and propagation properties of thermoacoustically coupled waves in one-dimensional ducts embedded with a periodic distribution of regenerators (REGs). In the following, we will refer to the acoustic waves supported by this type of waveguide as *TA Bloch waves*. This specific type of 1D waveguide can be seen as a form of semiactive acoustic metamaterial where TA energy conversion occurs periodically when the fluid passes through the evenlyspaced regenerators. The semiactive nature of the system is due to the fact that energy is either provided or extracted from the acoustic wave as a consequence of the imposed static thermal gradient on the REGs. The REG (also known, in more traditional TA studies, as the stack) consists of a porous material specifically designed to facilitate TA energy conversion. Indeed, from TA principles, it is well-known that the energy conversion is particularly significant when in the presence of a spatial temperature gradient imposed on the REG; a common setup for TA engine applications [20–23]. In the following, we will show that, other than powering

---
[*]haoh@purdue.edu
[†]Corresponding author: fsemperl@purdue.edu

TA engines, the TA coupling can also be leveraged to manipulate the propagation of TA Bloch waves and to shape its dispersion.

One of the most immediate consequences of the periodic exchange of TA energy and of the isothermal condition imposed on the REGs is the nonconservative nature of the periodic TA waveguide, which ultimately can lead to either an effective lossy or amplifying medium. The occurrence of a specific behavior depends on the direction of propagation of the wave with respect to the thermal gradient. While every natural material includes, to some level, nonconservative effects (the most immediate in solids being the mechanical energy dissipation associated with structural damping), these effects were often deemed negligible, so the early literature on periodic media and metamaterials had predominantly focused on the analysis of lossless conservative media. In this context, the classical dispersion analysis led to a real-valued band structure (RBS) for all propagating modes. In recent years, however, the intentional use of nonconservative effects has started drawing considerable attention and has established itself as a possible way to further manipulate the wave propagation characteristics of the host medium. Typical examples consist of metamaterial systems exploiting viscoelastic inserts [24–26] or dissipative periodic acoustic waveguides [27,28]. For this class of lossy materials, the RBS approach was not applicable, hence requiring a complex-valued band structure (CBS) approach [24]. In CBSs, the real part of the solution characterizes the propagating waves, while the imaginary part captures either the dissipation or the spatial attenuation of the waves.

As previously mentioned, in TA systems a significant energy exchange occurs between the mechanical component (carried by the acoustic wave) and the thermal component (produced by the heat source), hence giving rise to nonconservative behavior. It follows that, as for the example of viscoelastic metamaterials [24], the analysis of the band structure in TA periodic systems will also require a CBS approach. In addition, and differently from viscoleastic metamaterials, TA periodic systems are also intrinsically nonreciprocal (due to the presence of the spatial thermal gradient on the REG). We will show that the CBS is still well equipped to capture the response of TA periodic systems and that its application allows uncovering the existence of an anomalous unidirectional energy transport phenomenon. The dispersion calculation will be followed by an analysis, in the long-wavelength limit, of the effective properties of the TA unit cell. For this analysis, we consider the waveguide (in the long-wave limit) as an acoustic Willis material. The effective density, compressibility, and Willis coupling parameters are calculated, which justifies the nonreciprocal behavior of the proposed TA waveguide. The CBS approach also allows calculating the direction-dependent refractive index, which reveals the ability of the TA metamaterial to act as a zero refractive index (in one direction) material. Interestingly, the refractive index and the bandwidth of the effective zero refractive index can be tuned by controlling the strength of the thermal gradient. This result suggests that TA waveguides could open a route to the development of tunable single (and, possibly, double) zero acoustic media to achieve, among others, energy squeezing and cloaking effects.
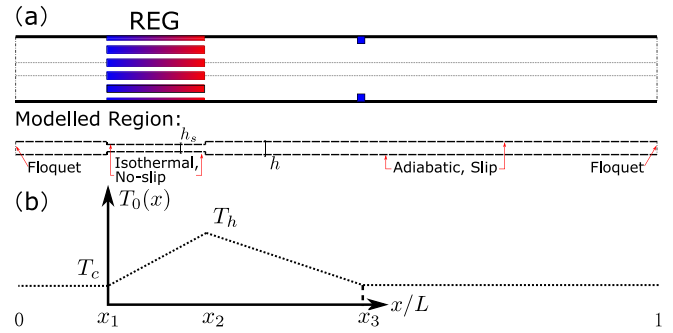

FIG. 1. (a) Schematic of the unit cell of the periodic thermoacoustic waveguide (top), and the section of the waveguide being modeled (bottom). (b) The mean temperature distribution along the unit cell. A spatial temperature gradient is imposed on the REG. An ambient heat exchanger is located at $x/L = x_3$.

Finally, but not less significant, the model approach and analysis proposed in this paper furthers the understanding of the amplification and attenuation characteristics of TA waves in the small-channel limit, which may have significant implications for the optimal design of TA amplifiers [19] and diodes [18] and, more in general, for TA engines in traveling wave configurations.

II. PROBLEM STATEMENT

The system under investigation consists of a one-dimensional infinite periodic waveguide whose fundamental unit cell is made of a straight duct and a REG [see Fig. 1(a)]. The REG can be thought of as a stack of short parallel plates separated by thin pores so, at low frequency, viscous and thermal conduction losses cannot be neglected. A temperature spatial gradient is imposed on the REG [Fig. 1(b)] to elevate the temperature from ambient temperature T_c at one end to the hot temperature T_h at the other end. The hot end of the REG is followed by a thermal buffer tube (TBT), terminated by an ambient heat exchanger that allows recovering the reference ambient temperature $T_c = T_{ref}$. The resulting temperature distribution in the unit cell is plotted in Fig. 1(b). Note that the TBT enables a continuity of temperature at the cell ends, while also acting as a local scatterer due to the temperature variation from T_{ref}.

To analyze the system, and without losing generality, we adopt a plane-wave assumption for the wave propagating in the 1D duct outside the REG. This same assumption is not valid for the waves inside the small pores of the REG due to the thermoviscous effects. Therefore, inside the REG channels, the solution is developed according to Rott's TA linear theory [20,29]:

$$\frac{dp}{dx} = -\frac{\rho_0}{1 - f_v}(i\omega)u, \tag{1}$$

$$\frac{du}{dx} = -\frac{1 + (\gamma - 1)f_k}{\gamma P_0}(i\omega)p + gu, \tag{2}$$

where

$$g = \frac{f_k - f_v}{(1 - f_v)(1 - \text{Pr})}\frac{1}{T_0}\frac{dT_0}{dx}. \tag{3}$$

u and p are first-order cross-sectionally averaged particle velocity and pressure, respectively. $\rho_0, P_0,$ and T_0 are zeroth-order (mean-state) density, pressure, and temperature, respectively. γ and Pr are specific heat ratio and Prandtl number, respectively. f_k and f_v are complex functions expressed as

$$f_\square = \frac{\tanh[(1+i)(h/2)/\delta_\square]}{[(1+i)(h/2)/\delta_\square]}, \qquad (4)$$

where $\square$ can take either the subscript of v or k. h is the width of the straight section. The viscous and thermal penetration depths are expressed as

$$\delta_v = \sqrt{2\nu/\omega}, \qquad \delta_k = \sqrt{2\kappa/\omega}, \qquad (5)$$

where ν and κ are the dynamic viscosity and the thermal diffusivity, respectively. Note that the thermoviscous coupling is particularly strong when the characteristic ratio $h/2\delta_\square$ is small. This latter condition can occur either when in presence of thin channels (i.e., small h) or of low frequency waves [i.e., large $\delta_\square$, Eq. (5)]. When the thermoviscous effects are negligible, that is, when $f_v = f_k = 0$, the Helmholtz equation is recovered from Eqs. (1) and (2). Considering the plane-wave assumption for the wide sections (outside the REG), as well as the fact that the pores in the REG are identical to each other, we simplify the modeling by only calculating the acoustic field in a minimal unit (including a single pore) [16], outlined by the dashed lines in Fig. 1. The Floquet boundary conditions are applied to the cell (minimal unit) ends:

$$u(L) = \exp(-ikL)u(0), \qquad (6)$$

$$p(L) = \exp(-ikL)p(0). \qquad (7)$$

Recall that the wave number k is complex-valued for the CBS analysis.

Mathematically, the CBS could be formulated in three different ways: (1) complex ω (frequency) versus real k (wave number), (2) real ω versus complex k, and (3) complex ω versus complex k. However, only the former two representations are physically significant. The first representation, appropriate for free wave propagation, considers a complex frequency $\omega = \text{Re}[\omega] + i\text{Im}[\omega]$ under a given real wave number k, where the imaginary part $\text{Im}[\omega]$ denotes the temporal growth ($\text{Im}[\omega] < 0$) or decay ($\text{Im}[\omega] > 0$) of the transient wave. The complex frequency is especially relevant to TA engines to describe the transient exponentially growing motion due to TA instability [30–34]. The imaginary part of ω is also widely used to represent the decay rate of the free vibration of a lossy material. The second representation is better suited for a time-harmonic wave propagation. The imaginary part of the complex wave number $k = \text{Re}[k] + i\text{Im}[k]$ allows capturing either the spatial attenuation or amplification of the time-harmonic wave at the steady state. In this paper, we adopt this latter (time-harmonic) description of a CBS in which a forcing frequency ω is taken as the real independent variable for the solution of a complex wave number $k = \text{Re}[k] + i\text{Im}[k]$ [24,35] to describe either the spatial amplification or attenuation of TA Bloch waves.

The discretization of Eqs. (1) and (2) (for the REG and for the duct, respectively) combined with the Floquet boundary

TABLE I. Geometrical and material parameters of the TA unit cell.

L[m]	h_s[mm]	h_s/h	x_1	x_2	x_3
0.5	0.25	0.75	0.1	0.12	0.45
P_0[Pa]	$T_c = T_{\text{ref}}$[K]	ρ_{ref}[kg/m^3]		Pr	γ
101325	300	1.2		0.72	1.4
$\mu(T_0)$[Pa · s] $= 1.98 \times 10^{-5}(T_0/T_{\text{ref}})^{0.76}$					

conditions [Eqs. (6) and (7)] yields a generalized eigenvalue problem,

$$[\mathbf{A} - \exp(-ikL)\mathbf{B}]\begin{bmatrix}\mathbf{p} \\ \mathbf{u}\end{bmatrix} = 0, \qquad (8)$$

where $\mathbf{A}$ and $\mathbf{B}$ are coefficient matrices in which certain elements are frequency related. The eigenfunction $[\mathbf{p}, \mathbf{u}]^{\text{T}}$ consists of the discrete distribution of pressure and velocity. Given the frequency ω, the eigenvalue $\exp(-ikL)$ can be obtained by applying any available eigenvalue solver. The complex wave number k can then be easily extracted. Repeating the process for different values of the frequency ω spanning a given range leads to the CBS of the system.

Recall that the TA coupling results from the combined effect of the thermoviscous behavior ($f_v \neq 0$ and $f_k \neq 0$) and of the temperature gradient along the REG ($T_h \neq T_c$). For a better understanding of the TA Bloch waves, we perform a CBS analysis of the waveguide under three configurations employing different assumptions: (1) pure acoustics (PA) or, equivalently, lossless acoustics ($f_v = f_k = 0$, $T_h = T_c$), (2) thermoviscous acoustics (TVA) ($f_v \neq 0$, $f_k \neq 0$, $T_h = T_c$), and (3) thermoacoustics ($f_v \neq 0$, $f_k \neq 0$, $T_h = 1.5T_c$). In all three cases, both the geometrical and the material properties are maintained the same, as listed in Table I. Cases (1) and (2) will serve as a reference to better understand the behavior observed in case (3) that represents the actual TA Bloch waves. Note that cases (1) and (2) are expected to be reciprocal due to the lack of the thermal gradient. In addition, in case (1) the imaginary part shall be nonzero only in the band gaps (it will be zero outside a band gap due to the lossless assumption).

III. RESULTS AND DISCUSSION

Figures 2(a) and 2(b) show the CBS of the periodic system under PA and TVA assumptions. Band gaps appear in Fig. 2(a.1) at the band crossings. Note that the pure acoustic case [Fig. 2(a)] still assumes slip wall conditions or, equivalently, no thermoviscous losses at the boundaries, but does not imply a uniform cross-section waveguide. These band gaps are the result of Bragg scattering occurring at the abrupt cross-sectional area changes at the REG ends [see Fig. 1(a) and note $h_s \neq h$]. The scattering is particularly strong when the length of the unit cell is approximately a multiple of the half wavelength [36]. $\text{Im}[k]$ is nonzero in the band gaps, indicating the presence of evanescent waves. The symmetry of the CBS also suggests that reciprocity is preserved. This behavior is clearly not surprising and consistent with the well-known response of classical nonresonant periodic media with periodic mechanical impedance mismatch. In the CBS plots,
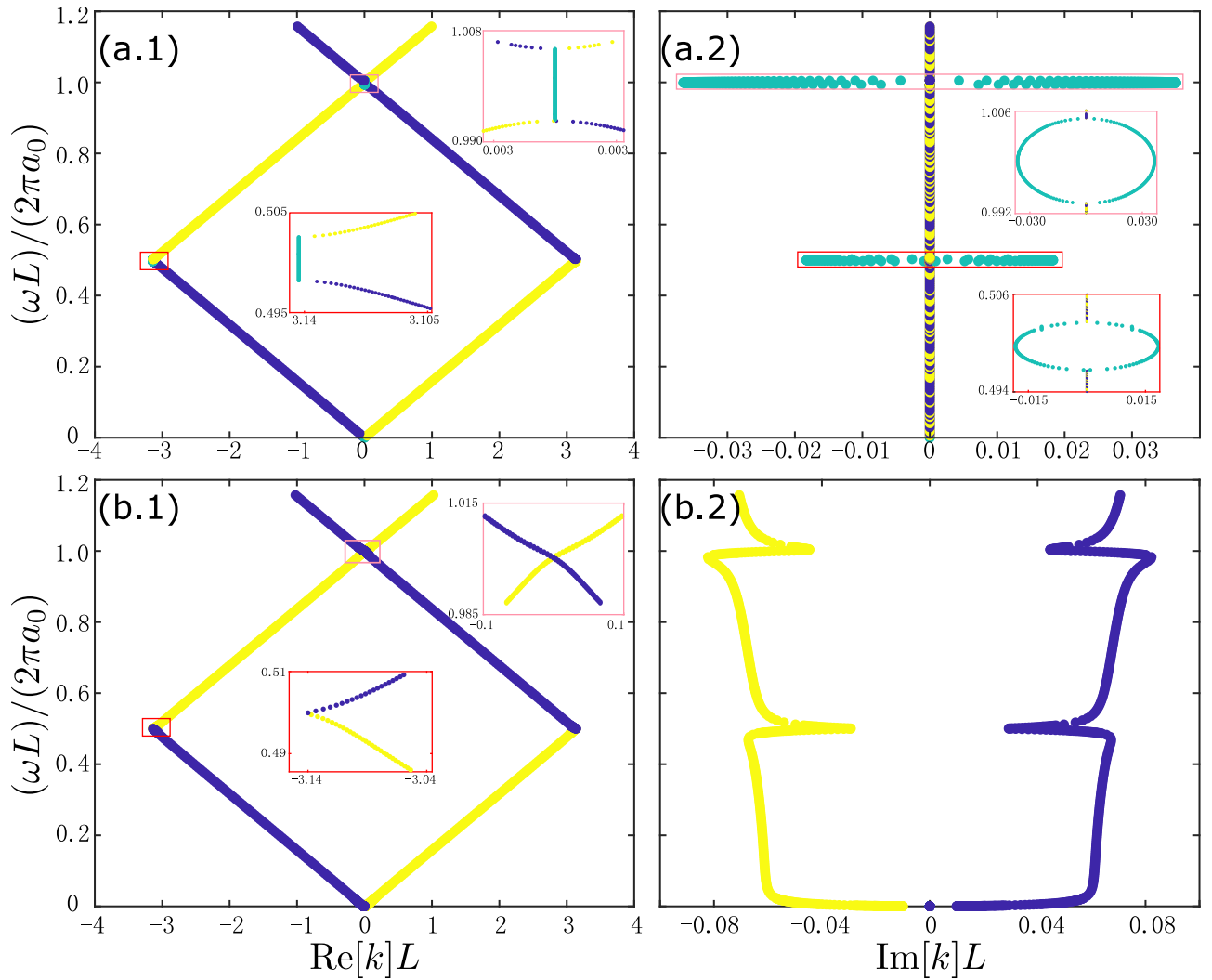
FIG. 2. Complex band structure of the unit cell under (a) pure acoustics ($f_k = 0$, $f_v = 0\, T_h = T_c$) assumption, and (b) thermoviscous acoustics ($f_k \neq 0$, $f_v \neq 0\, T_h = T_c$) assumption. Reciprocity is preserved under both assumptions. The vertical axis is the reduced frequency, where a_0 is the ambient sound speed at room temperature T_c, i.e., $a_0 = \sqrt{\gamma P_0 / \rho_{\text{ref}}} = 343$[m/s]. The curves are color coded based on the direction of the intensity, i.e., sgn(I), where yellow and blue colors denote sgn(I) = 1 and sgn(I) = −1, respectively.

modes are colored by the sign of the cycle-averaged acoustic intensity. The intensity is expressed as $I = 0.5\text{Re}[p\bar{u}]$, where the overbar denotes complex conjugate quantities. Remember that the sign of the acoustic intensity indicates the direction of the acoustic energy transport. The colors yellow and blue represent positive and negative intensity, while the green color denotes a zero intensity (which only appears for evanescent modes). The band gaps in Fig. 2(a.1) disappear in Fig. 2(b.1) due to the significant thermoviscous losses in the REG pores. The symmetrical distribution of k is still preserved in these configurations [Figs. 2(b.1) and 2(b.2)] because the temperature gradient is not activated. It is worth mentioning that the viscous and heat-conduction losses break time-reversal symmetry but do not affect reciprocity. It is also notable that in Fig. 2(b.2) all nonzero Im[k] correspond to spatial attenuation. Considering the $\exp(-ikL)$ notation for the Floquet boundary conditions, a forward-propagating wave (with positive intensity, yellow) attenuates along x if Im[k] < 0, while a backward-propagating wave (with negative intensity, blue) attenuates along $-x$ if Im[k] > 0.

A. Nonreciprocity and Willis coupling

Following the initial assessment of the dispersion behavior enabled by the CBS approach, Figures 3(a) and 3(b) show the real and imaginary parts of the CBS (indicated, in the following, as Re[CBS] and Im[CBS]) of the TA Bloch waves under TA coupling ($f_v \neq 0$, $f_k \neq 0$, $T_h = 1.5T_c$). Focusing on the Re[CBS], we observe that the band crossing that in the (reciprocal) thermoviscous case [Fig. 2(b.1)] occurred at Re[kL] = $\pm\pi$ is now shifted to Re[kL] = −3.07; as a consequence, an opening appears around π in the symmetric half of the first Brillouin zone (BZ) [see Fig. 3(a.2)]. The shift of the band crossing is a direct result of non-reciprocal wave propagation.

Recall that, under the thermoviscous assumptions, either a forward- or backward-propagating wave [marked in yellow or blue in Fig. 2(b), respectively] is always associated with either a negative or positive Im[k], which indicates spatial attenuation along the direction of propagation of the wave. Unlike the thermoviscous case, in the TA case the forward-
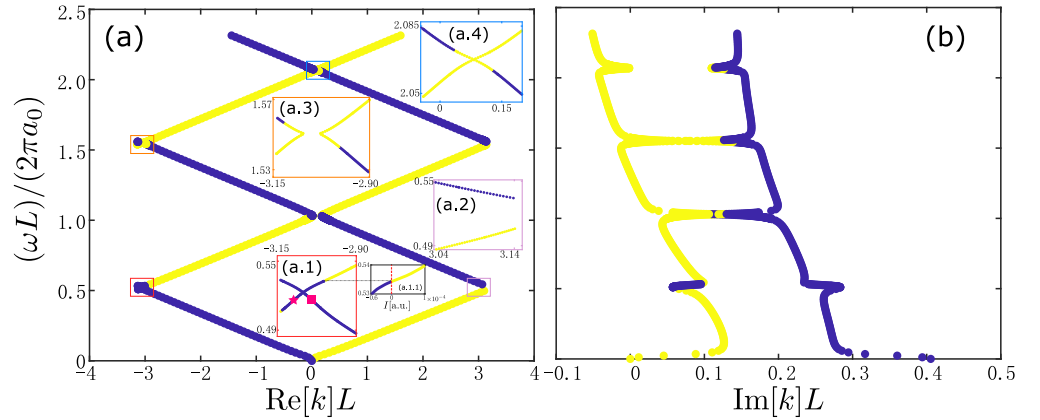
FIG. 3. Complex band structure of the unit cell under thermoacoustic ($f_k \neq 0$, $f_v \neq 0$ $T_h = 1.5T_c$) assumption. Reciprocity is broken, indicated by the asymmetric CBS. The star and the square in (a.1) denote two modes at the same frequency with opposite direction of group velocity, yet the same direction of intensity (same color). The acoustic impedance of these two modes will be plotted in Fig. 7. The inset (a.1.1) shows that the intensity evolution with frequency is continuous while the abrupt color change is due to the adoption of the sign function. a.u.: arbitrary unit.

propagating waves can be spatially amplified if $T_h \neq T_c$. This latter condition is indicated by yellow dots with positive Im[k] in Fig. 3(b). At the same time, the backward-propagating wave still attenuates along $-x$, according to the positive Im[k]. Such asymmetric nonconservative behavior (characterized by either attenuation or amplification) is a distinctive feature of the nonreciprocal response of TA Bloch waves. The nonreciprocal nature of thermoacoustically coupled devices (not necessarily periodic) is well documented in the literature. In finite systems, such as loop-shaped traveling wave engines, the two counterpropagating modes interfere asymmetrically (due to the TA coupling occurring in the REG) and cannot give rise to a standing wave. The resulting wave obtained by the superposition of the two counterpropagating waves moves in the direction of the rising temperature profile imposed on REG [14,15,37]. When applied to periodic structures, the nonreciprocal nature of the TA coupling has been shown in both TA diodes [18] and amplifiers [19]. In this paper, our focus was to formalize the description and behavior of propagating waves in periodic thermoacoustically coupled waveguides and to identify potential ranges of anomalous behavior. Our approach captured the (expected) nonreciprocity by performing a CBS analysis which highlighted the asymmetry of the dispersion relations.

A more analytical explanation of the nonreciprocal behavior of the TA waveguide can be established by realizing that the TA waveguide effectively behaves as a nonreciprocal 1D Willis material. Considering a general 1D acoustic wave with Willis coupling, the governing equations are written as [38,39]

$$\frac{dp}{dx'} = -i\omega\rho_{\text{eff}}u - i\omega\eta_{\text{eff}}p, \tag{9}$$

$$\frac{du}{dx'} = -i\omega\beta_{\text{eff}}p - i\omega\gamma_{\text{eff}}u, \tag{10}$$

where ρ_{eff} and β_{eff} are effective density and compressibility, η_{eff} and γ_{eff} are Willis coupling coefficients. These four effective parameters define the macroscopic characteristics of a Willis material, whose practical realization often involves repeating and heterogeneous micro-structures. x' denotes the coordinate of the homogenized 1D Willis material. A Willis material is nonreciprocal if and only if $\eta_{\text{eff}} + \gamma_{\text{eff}} \neq 0$ [38,39]. By considering the infinite TA waveguide as an effective Willis material, the four parameters can be calculated by [see Eqs. (9) and (10)]

$$\begin{bmatrix} \rho_{\text{eff}} \\ \beta_{\text{eff}} \\ \eta_{\text{eff}} \\ \gamma_{\text{eff}} \end{bmatrix} = \frac{i}{\omega L} \begin{bmatrix} \langle u_1 \rangle & 0 & \langle p_1 \rangle & 0 \\ 0 & \langle p_1 \rangle & 0 & \langle u_1 \rangle \\ \langle u_2 \rangle & 0 & \langle p_2 \rangle & 0 \\ 0 & \langle p_2 \rangle & 0 & \langle u_2 \rangle \end{bmatrix}^{-1}$$
$$\times \begin{bmatrix} p_1(L) - p_1(0) \\ u_1(L) - u_1(0) \\ p_2(L) - p_2(0) \\ u_2(L) - u_2(0) \end{bmatrix}, \tag{11}$$

where subscripts 1 and 2 denote the two eigenmodes extracted from the solution to the eigenvalue problem, Eq. (8). Also see the Appendix for more details. $\langle \rangle$ denote the spatial average of the field variables p and u. The spatial derivatives in the homogeneous Willis material ($d\diamond/dx'$) [Eqs. (9) and (10)] is approximated as the finite difference of the field variables evaluated at the two ends of the TA unit cell, i.e., $d\diamond/dx' = \diamond(L) - \diamond(0)/L$, where $\diamond$ takes the role of a field variable, either p or u.

Figures 4(a)–4(d) present the real (blue, solid) and imaginary (orange, dashed) parts of ρ_{eff}, β_{eff}, η_{eff}, and γ_{eff}, respectively. The interpretation of the effective properties can be more easily performed by comparing Eqs. (9) and (10), which govern the effective Willis material, and Eqs. (1) and (2), which govern the REGs in the TA waveguide. Clearly,
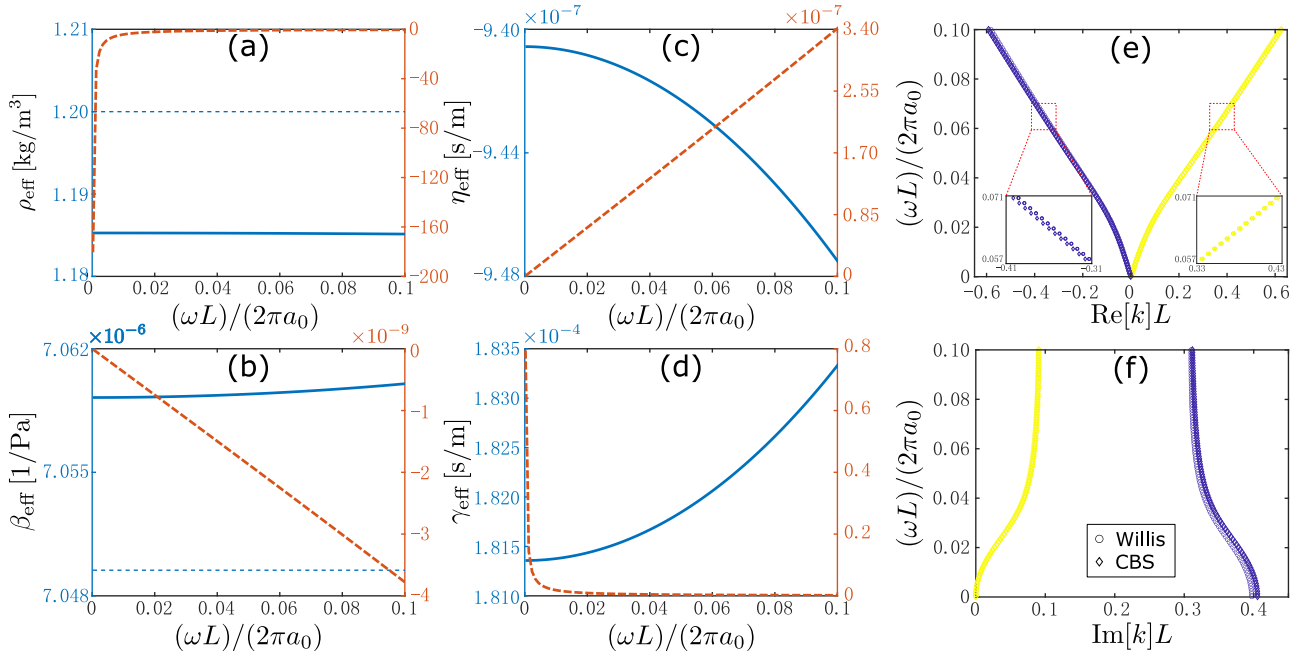
FIG. 4. Real (blue, solid) and imaginary (orange, dashed) parts of (a) effective density $\rho_{\rm eff}$, (b) effective compressibility $\beta_{\rm eff}$, and (c), (d) effective Willis coupling coefficients $\gamma_{\rm eff}$ and $\eta_{\rm eff}$ of the TA waveguide, in the long-wavelength limit. The thin blue dashed lines in (a) and (b), shown as references, denote the static density and compressibility of ambient air at room temperature. (e), (f) The real and imaginary parts of the dispersion relation calculated by the Willis effective model via Eq. (12) (circle), and by the CBS approach (diamond). Note that the curves calculated by the CBS approach (diamonds) is the same shown in Fig. 3 in the range of $(\omega L)/(2\pi a_0) \in [0, 0.1]$.

the deviation of the effective properties from their reference values, which are the corresponding properties of ambient air at room temperature, is mainly attributed to the TA coupling in the REG. Such coupling is accomplished through the parameters f_v, f_k, and g in Eqs. (1) and (2). The difference between Re$[\rho_{\rm eff}]$ and $\rho_{\rm ref} = 1.2[{\rm kg/m}^3]$ is the result of two main factors: (1) the temperature dependence of the mean density ρ_0 and (2) the diffusion-induced effect, specifically the viscous effect, f_v. Note that $f_\square$ is a complex-valued quantity. The slight difference between Re$[\beta_{\rm eff}]$ and $\beta_{\rm ref} = 1/\gamma P_0 = 7.049 \times 10^{-6}[1/{\rm Pa}]$ arises only due to the complex valued f_k because we assume γP_0 as temperature-independent quantities in our model. The complex-valued $f_\square$ also gives rise to the imaginary parts of $\rho_{\rm eff}$ and $\beta_{\rm eff}$. The significant value of Im$[\rho_{\rm eff}]$ suggests that the viscous effect (induced by f_v) is particularly strong in the low frequency. Turning to the analyses of the Willis coupling parameters $\eta_{\rm eff}$ and $\gamma_{\rm eff}$ (remember these two parameters have the same units), it is easily observable from Figs. 4(c) and 4(d) that Im$[\gamma_{\rm eff}]$ is significantly larger than Re$[\gamma_{\rm eff}]$, Re$[\eta_{\rm eff}]$, and Im$[\eta_{\rm eff}]$, so the latter three quantities are effectively negligible. From Eqs. (1) and (2), we reach the following observations: (1) no explicit coupling between (dp/dx) and $i\omega p$ appears in the REG, leading to a negligible $\eta_{\rm eff}$; (2) the coupling term gu contributes to the significant Im$[\gamma_{\rm eff}]$ because $(g/i\omega)$ is dominated by its imaginary part in the long-wavelength limit [when ω is small. See Eqs. (3) and (4)].

To validate the adopted homogenization method [Eq. (11)], we calculate the dispersion relation of the effective medium [40],

$$k_{\rm eff} = \frac{\omega}{2}[\eta_{\rm eff} + \gamma_{\rm eff} \pm \sqrt{(\eta_{\rm eff} - \gamma_{\rm eff})^2 + 4\rho_{\rm eff}\beta_{\rm eff}}], \quad (12)$$

using the effective properties calculated via Eq. (11). The dispersion relation of the effective Willis material calculated via Eq. (12) is plotted in Figs. 4(e)–4(f) and compared with the dispersion of the TA waveguide calculated by the CBS approach introduced earlier. The agreement between the two solutions is excellent, hence justifying the assumption that the TA waveguide can be effectively modeled, in the long-wavelength limit, as an acoustic Willis material.

From Figs. 4(c) and 4(d), it immediately follows that $\eta_{\rm eff} + \gamma_{\rm eff} \neq 0$ for all frequencies in the displayed range, which supports the observation from the numerical dispersion analysis (the CBS approach) that the proposed TA waveguide is non-reciprocal. This result is indeed in line with previous studies [38] that have used external actions, such as a fluid flow [1] or a magnetic field [41], to break reciprocity. In our proposed waveguide, the external action is provided by the static temperature gradient which affects the acoustic wave by means of the TA coupling. We merely note that, although the simplified homogenization approach [Eq. (11)] is sufficient to calculate the effective properties of the effective Willis material, there exist other more advanced homogenization approaches specifically developed for elastic and acoustic materials in the literature. See, for example, Refs. [42–45].

We highlight that the nonreciprocal propagation can be effectively exploited to achieve an effective one-way sound transmission in the 1D TA waveguide. Figure 5 shows the simulated results of a pressure pulse applied at the center of a finite length waveguides consisting of 30 unit cells. The propagation of the pulse is studied for the three configurations discussed above, that is, PA, TVA, and TA described in Sec. II. Clearly, in the PA and TVA cases, the pulse splits in two equal parts that propagate in opposite directions, hence
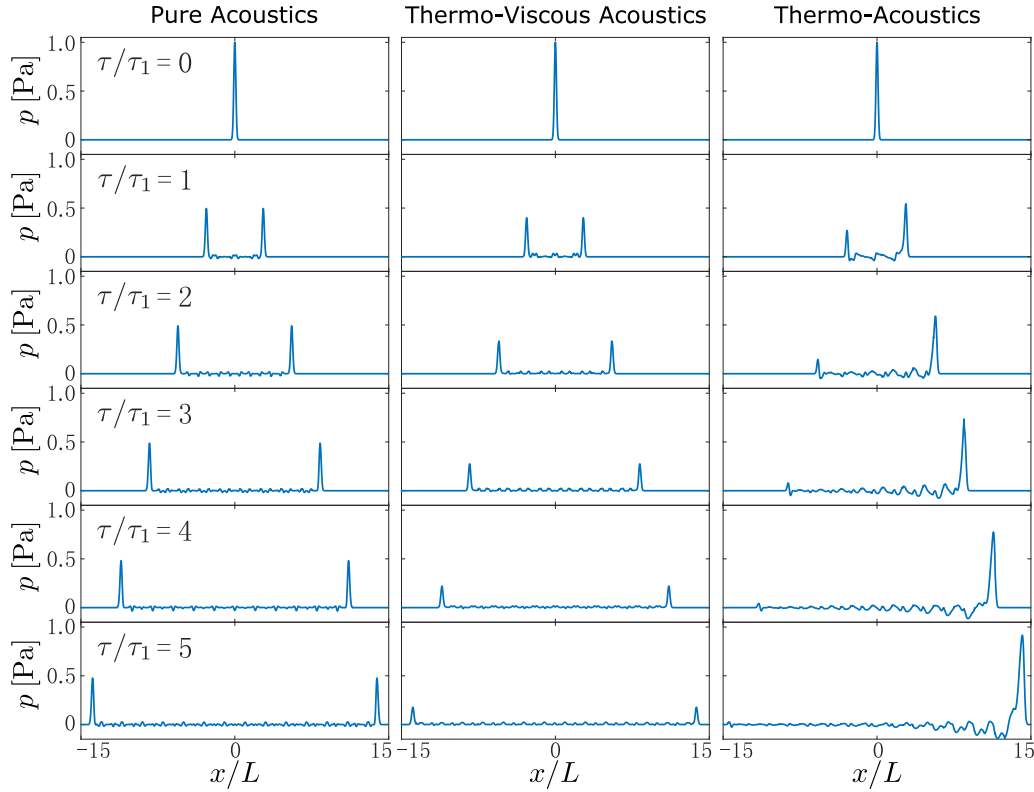
FIG. 5. A pressure pulse is applied in the center of a 30-unit TA periodic waveguide. The pulse splits into two fronts propagating in opposite directions. The propagation characteristics are studied for the three different cases previously defined, that is pure acoustic (PA), thermoviscous-acoustic (TVA), and thermoacoustic (TA) assumptions, respectively. In the PA and TVA cases, the two fronts propagate in opposite directions and the response remains symmetric. The TVA response shows amplitude attenuation due to the thermoviscous losses. In the TA case, the forward-propagating front is amplified while the backward-propagating one is attenuated due to the TA coupling. The combined effect results in an effective nonreciprocal, unidirectional sound propagation. The small fluctuations near $p = 0$ are due to the intercell reflections. τ indicates time and $\tau_1 = 0.004$[s].

maintaining a symmetric and reciprocal behavior. The same situation occurs for the TVA configuration, however, the two pulses experience a spatial attenuation due to thermoviscous losses. The small fluctuations near $p = 0$ are due to the intercell reflections. In the TA case, after the initial pulse separates into two fronts, the forward-propagating front is spatially amplified while the backward-moving one is attenuated. The spatial amplification of acoustic waves relies on the heat provided to the system at the hot side of REG. The amplitude of the amplified pulse will eventually reach a steady state value, balanced by nonlinear saturation [16,46]. It follows that, in the far field, only the forward-propagating pulse survives while the backward one disappears. This one-directional, nondecaying propagation may find interesting applications in long-range acoustic communication [47]. The spatial amplification of time-harmonic waves in a waveguide formed by a cascade of several unit cells had been experimentally demonstrated in Refs. [18,19], although without providing the underlying theoretical framework. We merely note that the ability of the TA propagating Bloch wave to reach a consistent value of the wave amplitude in the far field, could effectively result in an equivalent cloaking behavior. Indeed, any reduction in the wave amplitude due to back scattering effects would be recovered, upon propagation, due to the TA coupling; hence not leaving any detectable trace of scattering in the far field.

B. Unidirectional energy transport

An inspection of the acoustic intensity associated with the TA coupled modes in the reduced frequency range $(\omega L)/(2\pi a_0) \in [0.51, 0.53]$ reveals that the intensity I of both modes has the same sign [Fig. 3(a.1)]. Recall that a_0 is the ambient sound speed in air, i.e., $a_0 = \sqrt{\gamma P_0/\rho_{\text{ref}}} = 343$[m/s]. In other words, the mode labeled with a star marker has positive group velocity yet negative intensity. This observation is certainly counterintuitive because in classical wave theory the group velocity is also understood as the direction of energy transport. The results suggest that, while a wave packet with the carrier frequency around $(\omega L)/(2\pi a_0) = 0.52$ propagates forward as a whole, the energy of the carrier frequency time-harmonic TA Bloch wave is transmitted along the direction of the intensity, that is, the $-x$ direction. Similar phenomena are also observed around the reduced frequency 1.55 and 2.07 [Figs. 3(a.3) and 3(a.4)], where both modes have positive intensity. The blue and yellow colors in Figs. 2 and 3 indicate the sign of the intensity. Specifically, modes with $\text{sgn}(I) = 1$ are colored yellow, while those with $\text{sgn}(I) = -1$ are colored blue. Therefore, the abrupt color change in the insets of Fig. 3 is simply an artifact of the sign function that switches suddenly as the function crosses zero. However, this does not imply that the evolution of the intensity is not
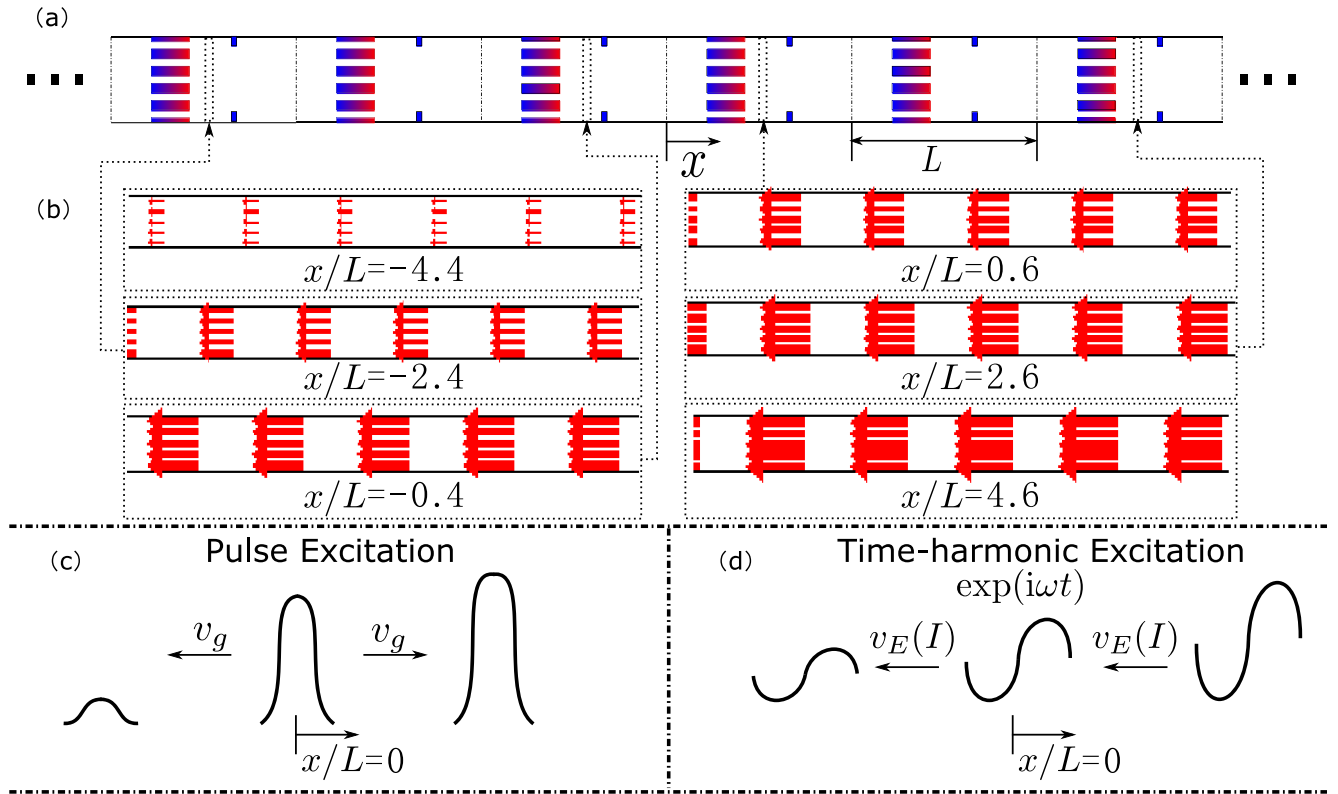
FIG. 6. (a) Schematic of a periodic TA waveguide including the REG and the ambient heat exchanger. The color gradient in the REG indicates the cold (blue) and hot (red) temperature side. The vertical dashed lines represent the separation between consecutive unit cells. The behavior of the waveguide is explored under either (c) pulse excitation or (d) time-harmonic excitation. (c) A pulse is generated at $x/L = 0$ and splits into two fronts. The two fronts, as well as the energy they carry, travel in opposite directions. The front traveling in the direction of the temperature rise ($x/L > 0$ region) is amplified, while the front moving in the opposite direction is attenuated, as shown in Fig. 5. (d) A time harmonic excitation is generated at $x/L = 0$ and propagates in both directions. However, at selected frequencies [e.g., the one represented by the star and square markers in Fig. 3(a.1)] both steady-state modes can transport energy unidirectionally toward $-x$. (b) The cycle-averaged acoustic intensity I associated with the time-harmonic wave is plotted at different locations along the periodic waveguide [highlighted by dashed boxes in (a)]. The direction and length of the arrows indicate the direction and log-scale amplitude of the acoustic intensity.

continuous. In fact, near the transition point, the intensity still continuously varies from a positive value to a negative value, or vice versa. To build the CBS, we swept the frequency ω in discrete increments, hence not capturing the exact points where the intensity crosses zero. To further clarify this point, we also plot in Fig. 3(a.1.1) the intensity I evaluated at $x = 0$ in a unit cell near a transition point.

The inconsistency between the group velocity v_g, also dubbed macroscopic energy transport velocity [48], and the microscopic energy transport velocity v_E associated with the acoustic intensity I in acoustic Bloch waves was examined by Bradley [48]. Note that v_E is proportional to I. For inviscid acoustic Bloch waves, the signs of v_E and v_g can differ due to the portion of energy stored in scattering elements eventually present on the wave path. In other terms, while the majority of the energy is transported by the wave in the same direction of propagation, a small portion of energy is stored in the wave scatterers. This part of the energy, termed *stagnant energy*, is not accounted for in the calculation of the microscopic energy transport velocity v_E. Indeed, the calculation of v_E only considers the portion of energy that is effectively in transport following the time-harmonic wave. On the other

side, the stagnant energy is considered in the calculation of v_g, which is a measure of the propagating speed of pulses or wave packets, as well as the energy carried by them. When the TA effect is taken into account, the discrepancy between v_g and v_E is affected by the thermoviscous effect as well as the TA energy production. Although it is the latter effect which mainly contributes to the occurrence of opposite signs for v_g and v_E (or, equivalently, I).

To further illustrate the characteristics of the energy transported by time-harmonic waves (at velocity v_E) and by a wave packet (at velocity v_g), we consider a periodic TA waveguide as shown in Fig. 6(a). A pulse initiated at $x/L = 0$ (and intrinsically composed of many harmonics) will split into two fronts and travel in both directions, with one front being amplified and the other being attenuated, as shown in Fig. 5. The energy carried by each front travels at a speed v_g [the slope of the curves in Fig. 3(a)] associated with these two fronts as schematically shown in Fig. 6(b). If a time-harmonic excitation is instead generated at $x/L = 0$ and at a selected frequency [represented by either the star or the square markers shown in Fig. 3(a.1)], the steady-state energy transfer shows different properties. Although the amplitude

of the time-harmonic wave increases in the direction of the rising temperature gradient or, equivalently, decreases in the opposite direction, the acoustic intensity always has a negative sign. In other terms, the energy always flows in the negative x direction. To provide further validation and insights in this unexpected result, we perform both 2D numerical finite-element analyses as well as theoretical investigations.

Starting with the numerical analyses, we developed a finite element model (FEM) (using the commercial software COMSOL MULTIPHYSICS) of a TA coupled periodic duct consisting of ten unit cells. An impedance type boundary condition was applied at both ends of the periodic assembly to reduce unwanted reflections. The impedance values were calculated using our theoretical model [Eq. (8)] for the specific modes selected [indicated by the star and square markers in Fig. 3(a.1)]. A unit amplitude time-harmonic velocity excitation was applied at $x/L = 0$. Figure 6(b) shows the acoustic intensity extracted from the data produced by the finite element model. The arrow direction and size (plotted in log scale) indicate the direction and magnitude of the intensity, respectively, at different locations along the periodic waveguide. It follows that the wave field on the right- and left-hand sides of the excitation correspond to the two modes indicated by the star and square markers in Fig. 3, respectively. Figure 6(d) shows that, on both sides of the time-harmonic excitation, the cycle-averaged intensities are negative. On the positive half region of the x axis ($x/L > 0$), the energy flows toward the mechanical source placed at $x/L = 0$ or, equivalently, the mechanical excitation behaves as an effective energy sink. This counterintuitive behavior is a result of the rectifying effect produced by the periodic distribution of REGs in the waveguide. We note that the proposed waveguide can be seen as an active material in the sense that the REGs provide energy to the acoustic waves. In other terms, the static temperature gradients applied to the REGs serve as energy sources (mediated by the TA coupling), hence continuously providing energy to the waveguide. At certain frequencies [for example, those shown in Fig. 3(a.1)], the energy provided by the heat source flows toward the negative x direction. Note also that the direction (sign) of intensity depends on the phase difference between p and u, or the PU phase. The expression of intensity can be further manipulated to yield $I = 0.5\text{Re}[p\overline{u}] = 0.5|p||u|\cos(\phi_p - \phi_u)$, where $|p|$ and $|u|$, and ϕ_p and ϕ_u are the magnitudes and phases of p and u, respectively. Therefore, a negative intensity implies the PU phase $(\phi_p - \phi_u) \in (\pi/2, 3\pi/2)$. The mechanism by which the REGs affect the PU phase is rather complex, but well explored in the TA literature (see for example, [49,50]). When the TA energy exchange is sufficiently strong, the direction of the acoustic energy flow (intensity) induced by solely the mechanical excitation is altered. As a result, the net intensity is negative, so the mechanical excitation appears as an energy sink. Recall that the arrow length in Fig. 6 is plotted in log scale. The analysis of the steady-state time-harmonic TA Bloch wave in the $x/L > 0$ range leads to the following conclusion: an oscillation amplitude at a point in the far field ($x/L > 0$) larger than the mechanical excitation amplitude ($x/L = 0$) does not necessarily indicate that the TA Bloch wave is spatially amplified. Indeed, in the $x/L > 0$ range, the time-harmonic wave is attenuated when traveling from the far field toward the mechanical excitation.

The mechanical excitation, for the time-harmonic wave in the $x/L > 0$ range, behaves as an energy sink.

The above considerations made on the ground of numerical results were also corroborated by a rigorous derivation of the relation between v_g and I. The derivation is provided here below.

Evaluating $d[\overline{p}'u + p\overline{u}']/dx$ yields

$$
\frac{d}{dx}[\overline{p}'u + p\overline{u}'] = E_{\text{ta}}
$$

$$
\begin{aligned}
&= \frac{i\rho_0}{1 - \overline{f_v}}(1 + \omega\frac{f_v'}{1 - \overline{f_v}})\overline{u}u \\
&\quad + \frac{i}{\gamma P_0}[1 + (\gamma - 1)\overline{f_k} + \omega(\gamma - 1)\overline{f_k}']\overline{p}p \\
&\quad + \frac{2\omega\rho0}{|1 - f_v|^2}\text{Im}[f_v]\overline{u'}u + \frac{2\omega}{\gamma P_m}(\gamma - 1) \\
&\quad \times \text{Im}[f_k]\overline{p'}p + gu\overline{p'} + \overline{gu'}p + \overline{g'}\overline{u}p, \quad (13)
\end{aligned}
$$

where E_{ta} is the mechanical energy distribution under TA coupling, the overbar denotes complex conjugate quantities and the prime denotes $\partial/\partial\omega$. Integrating Eq. (13) over the unit cell and incorporating the Floquet boundary conditions [Eqs. (6) and (7)] yield

$$
4iL\frac{\partial\overline{k}}{\partial\omega}\{\tfrac{1}{4}[\overline{p}(0)u(0) + \overline{u}(0)p(0)]\}\exp(2\text{Im}[k]L)
$$

$$
= -[\overline{p'}(0)u(0) + \overline{u'}(0)p(0)]\exp(2\text{Im}[k]L - 1) + \int_0^L E_{\text{ta}}dx. \tag{14}
$$

Recall that

$$
v_g = \frac{\partial\omega}{\partial\text{Re}[k]} = 1/\text{Re}\left[\frac{\partial\overline{k}}{\partial\omega}\right], \tag{15}
$$

$$
I = \text{Re}\{\tfrac{1}{4}[\overline{p}(0)u(0) + \overline{u}(0)p(0)]\}. \tag{16}
$$

For propagating pure acoustic waves ($\text{Im}[k] = 0$, $f_v = f_k = 0$, and $T_h = T_c$), Eq. (14) becomes

$$
I/v_g = \langle E \rangle = \frac{1}{4L}\int_0^L (\rho_0|u|^2 + \frac{1}{\gamma P_m}|p|^2)dx, \tag{17}
$$

where $\langle E \rangle$ denotes the spatially averaged mechanical energy along the unit cell. Equation (17) is consistent with the observation that the intensity of a propagating time-harmonic acoustic plane wave is always in the same direction as its group velocity. However, the existence of thermoviscous losses (nonzero f_v and f_k) as well as of the temperature gradient (nonzero g) gives rise to the discrepancy between the sign of v_g and I [Eq. (14)].

To further substantiate the previous finding, we plot the acoustic impedance distribution $z = p/u$ (which is scale-independent) along the unit cell for the two modes at $(\omega L)/(2\pi a_0) = 0.52$ in Fig. 7. The results are compared with a fully numerical FE solution obtained via COMSOL. The numerical model represents a single pore, as outlined in Fig. 1(a), with parameters given in Table I. Similar to the other numerical FE simulations presented in the earlier part of the section, the right end of the duct was subject to an impedance
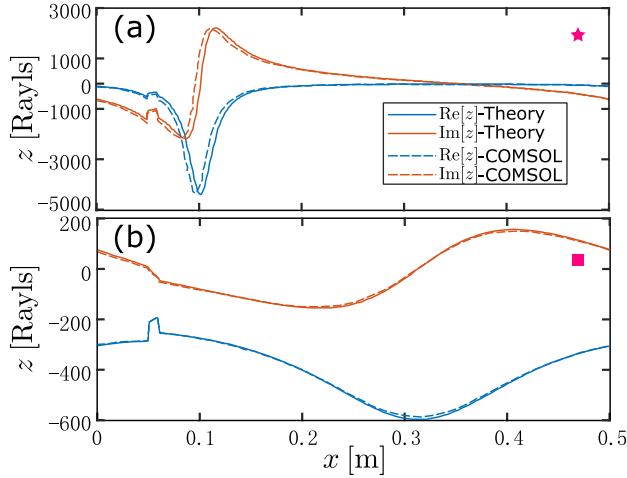
FIG. 7. Real and imaginary parts of the impedance $z = p/u$ of the two modes at reduced frequency $(\omega L)/(2\pi a_0) = 0.52$, denoted by the star and the square in Fig. 3(a.1). Both modes show negative $\text{Re}[z]$, denoting negative intensity I.

boundary condition. The complex-valued impedance was extracted from our theoretical results. The duct was excited by applying a unit-amplitude pressure at the left end. The model was used to calculate the steady-state response and to extract the impedance distribution along the waveguide. The results reported in Fig. 7 show very good agreement between the finite element solution and our theoretical calculations. Recalling that $\text{Re}[z] = I/|u|^2$, the negative $\text{Re}[z]$ confirms the occurrence of negative intensity for both modes, hence unidirectional energy transport within the frequency range of $(\omega L)/(2\pi a_0) \in [0.51, 0.53]$.

C. Unidirectional zero refractive index

In this section, we further explore the wave propagation characteristics of the TA waveguide by analyzing the refractive index of the TA Bloch wave. It was discussed above as the CBS approach allows calculating the complex dispersion relation associated with an input frequency ω. The refractive index is easily obtained by its definition $n = k/\omega$, where $k = \text{Re}[k] + i\text{Im}[k]$ is the complex wave number extracted from the CBS analysis. Due to the nonreciprocity of the TA waveguide, as shown in Sec. III A, the CBS is asymmetric, i.e., $k_1 + k_2 \neq 0$, leading to $n_1 + n_2 \neq 0$. We will show that, in selected frequency ranges, the TA waveguide is capable of zero refractive index in one direction. In zero index media, acoustic waves can propagate without phase variation, which in turn can lead to acoustic devices exhibiting intriguing properties [51,52] such as acoustic cloaking and energy squeezing [53] and acoustic superlenses [54]. Double zero properties (i.e., simultaneous zero effective density and effective compressibility) are typically required for an efficient preservation of both phase and amplitude profiles of the acoustic wave front when interacting with scatterers or geometric inhomogeneities. However, also single zero media (i.e., zero compressibility) have shown to be able to preserve the phase profile [51,52].
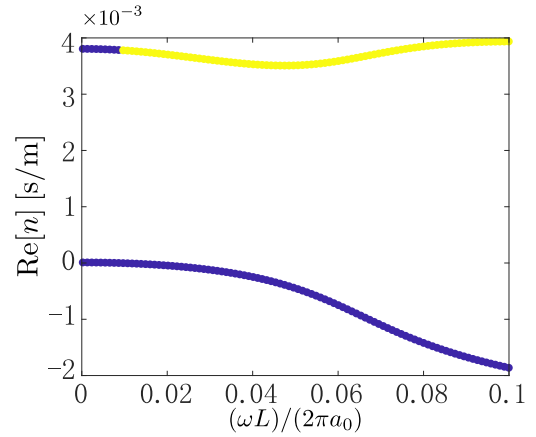

FIG. 8. Real part of the refractive index $\text{Re}[n] = \text{Re}[k]/\omega$ of the TA waveguide. The design parameters for the TA unit cell are given by: $x_1 = 0.485$, $x_2 = 0.515$, $x_3 = 0.545$, $h_s = 0.96[\text{mm}] = 5.714h$, and $T_h/T_c = 3$.

To clearly illustrate the occurrence of the zero refractive index, we modify the design parameters for the TA unit cell to the following values: $x_1 = 0.485$, $x_2 = 0.515$, $x_3 = 0.545$, $h_s = 0.96[\text{mm}] = 5.714h$, and $T_h/T_c = 3$. Figure 8 shows the real refractive index in the long-wave limit. It clearly shows that the lower mode (the $\text{Re}[n] < 0$ branch) has near-zero index behavior when ω is small, which is indicative of invariant phase. Note that, in this discussion, we focus on the propagating characteristics of the TA Bloch wave, which is reflected by $\text{Re}[n]$. Nevertheless, due to diffusion mechanisms associated with the TA coupling, the nonconservative behavior may lead to a nonzero $\text{Im}[n]$, as an indicator of the spatial attenuation or amplification of the TA Bloch wave, which will be further discussed in Sec. III D.

Figure 8 also shows that, as $\omega \to 0$, the intensity associated with both modes become negative (denoted by blue curves in Fig. 8), which is a sign of unidirectional energy transport. This aspect has been discussed in detail in Sec. III B. When occurring in the long-wavelength limit ($\omega \to 0$), such unidirectional behavior can also be justified by considering the TA waveguide as a homogeneous Willis material. From Eqs. (9) and (10), the phase difference ($\phi_p - \phi_u$) is expressed as

$$\phi_p - \phi_u = \arg\left[\frac{\omega\rho_{\text{eff}}}{k_{\text{eff}} - \omega\eta_{\text{eff}}}\right] = \arg\left[\frac{k_{\text{eff}} - \omega\gamma_{\text{eff}}}{\omega\beta_{\text{eff}}}\right]. \quad (18)$$

Note that the relation $d/dx' \to (-ik_{\text{eff}})$ is used when deriving Eq. (18) from Eqs. (9) and (10). It has been shown in Sec. III B that a negative intensity implies PU phase $(\phi_p - \phi_u) \in (\pi/2, 3\pi/2)$. Using Eq. (18), the PU phase corresponding to the two modes plotted in Fig. 8 at the reduced frequency $(\omega L)/(2\pi a_0) = 0.003$ is evaluated as $(\phi_p - \phi_u) = -1.714[\text{rad/s}]$ (top mode in Fig. 8) and $(\phi_p - \phi_u) = -1.590[\text{rad/s}]$ (bottom mode), respectively, both within the range of $(\phi_p - \phi_u) \in (\pi/2, 3\pi/2)$, which is indicative of the unidirectional energy transport (in the negative x direction). The consistent observations of the unidirectional energy (intensity) transport developed from both the effective Willis medium approach and the CBS approach (Fig. 8) again show
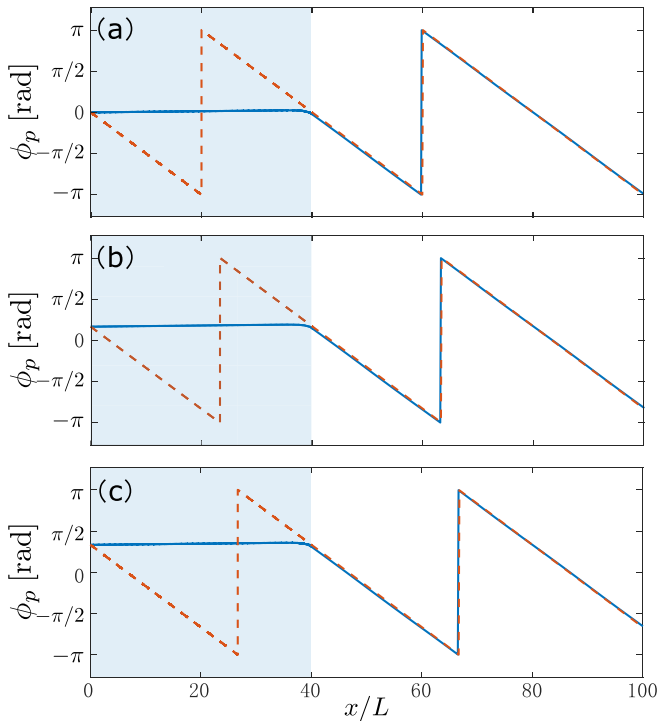
FIG. 9. Phase of pressure along the center line of the designed waveguide with TA section (solid) and a hollow duct filled with ambient air as a reference (dashed). The input phase θ is (a) 0, (b) $\pi/6$, and (c) $\pi/3$. The shaded region represents the TA section.
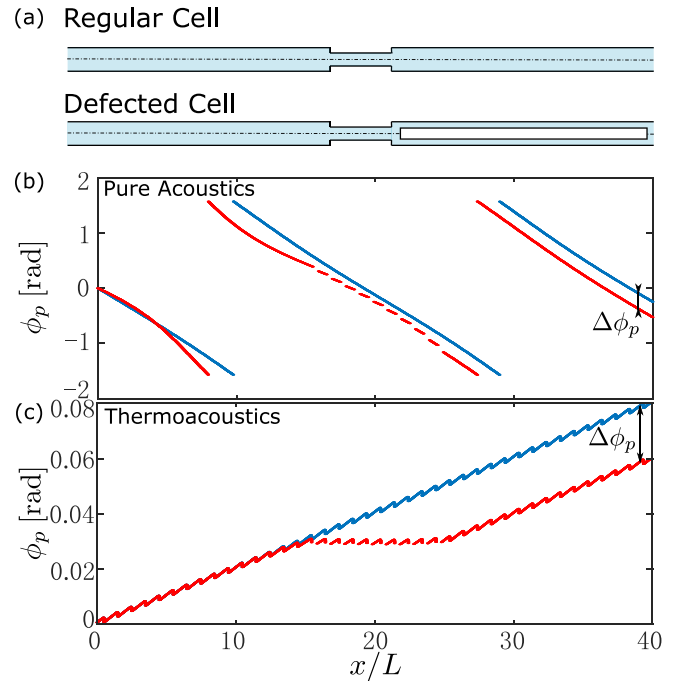

FIG. 10. (a) Schematic of a (top) regular unit cell without defect, and (bottom) a defected unit cell with a rectangular sound hard scatterer. (b), (c) Pressure phase distribution along the centerline [dashed line in (a)] of the 40-cell waveguide under (b) pure acoustic, and (c) thermoacoustic assumptions. The blue and red phase is associated with the regular and the defected waveguide, respectively. The dashed sections in the red curves denote the location of the ten defected cells.

the validity of the homogenization approach of the TA waveguide as an effective Willis medium.

Getting back to substantiating the observation of the occurrence of the zero refractive index, we performed a numerical simulation of the steady-state harmonic response of the waveguide via finite element modeling. The waveguide consists of 40 TA unit cells ($x/L \in [0, 40]$) followed by a homogeneous hollow duct ($x/L \in [40, 100]$) filled with ambient air. The hollow duct is $60L$ long and it is terminated at $x/L = 100$ with an impedance boundary condition that matches the impedance of air (415 [Rayls]) to eliminate reflections. The waveguide is excited at $x/L = 0$ with a pressure $p = \exp(i\theta)$ at frequency $f = 17.15$[Hz]. Note that this excitation at $x/L = 0$ is selected to only excite the mode that exhibits the phase-invariant transition [Fig. 11(b)]. The solid lines in Fig. 9 show the phase of the pressure field $\phi_p(x) = \arg(p(x))$ along the center line of the waveguide following different input phases $\theta = 0$, $\pi/6$, and $\pi/3$. The shaded area denotes the section of the waveguide taken by the 40 TA unit cells. The dashed lines show a baseline phase profile that would be obtained if the TA section were substituted by a hollow duct filled with ambient air (that is, the entire $100L$ long waveguide would consist of a hollow duct filled with air). Results clearly show that, under near zero refractive index conditions, the phase remains invariant within the TA section, regardless of the input phase.

An important feature of zero-index materials is that possible defects inside the waveguide do not alter significantly the phase profile [51,53]. The concept of acoustic cloaking strongly relies on this feature. To further corroborate the phase

invariant characteristic of the proposed TA waveguide and its insensitivity to internal defects or scatterers, we performed numerical simulations on an acoustic waveguide composed of 40 unit cells, ten of which included defects. More specifically, we considered a baseline configuration made of 40 unit cells without defects (essentially equivalent to the TA waveguide discussed above), and a second configuration in which ten unit cells in the middle included a defect. The defect consisted of a rectangular sound hard scatterer ($0.39L$ long and $0.5h$ wide), as shown in Fig. 10(a). The structure was excited at $x/L = 0$ with a zero-phase, unit-amplitude pressure that is $p = \exp(i0)$. Impedance matching condition was applied to the other end of the structure ($x/L = 40$). The remaining geometrical parameters and the applied temperature gradient were unchanged with respect to the results presented in Fig. 9.

Results are presented in Fig. 10 in terms of phase profile of the pressure field along the centerline [dashed line in Fig. 10(a)] of the 40-cell structure. Figure 10(b) shows the pure acoustic case (i.e., without TA coupling) which provides a reference baseline. The blue and red curves denote the phase along the regular and the defected waveguide, respectively. Based on these results, it is seen that, in the region downstream of the defects, a 0.26 rad ($\approx 15°$) phase difference $\Delta\phi_p$ is induced due to the presence of the defects. Contrarily, when the TA coupling is activated, the shift in phase $\Delta\phi_p$ is reduced to 0.02 rad ($\approx 1°$), as shown in Fig. 10(c). This drastic reduc-

tion leads to an overall phase shift that is negligible in practical applications. We conclude that, as expected based on the previously discussed effective properties, the TA waveguide is capable of maintaining an effective invariant phase transition, a necessary condition for acoustic cloaking. We merely note that the TA waveguide is incapable of impedance matching, a key feature of double-zero materials for high transmission and cloaking [51,53]. An interesting phenomenon can take place in this class of waveguides thanks to the multiphysics coupling and to the energy provided to the system by the thermal sources (at the REG locations). Indeed, it was previously shown that the wave traveling in the direction of the rising temperature gradient can be effectively amplified. We also know that, in TA systems, sound amplification (due to the underlying TA instability) is balanced by nonlinear losses, ultimately allowing reaching a steady-state response [16,20]. It is possible to envision that, under these conditions, the amplitude decrease in the transmitted wave (due to the scattering element) can be recovered due to the TA coupling. This means that, in the far field (downstream of the scattering section), the response of the two waveguides (i.e., the baseline and the TA configurations) would be exactly identical (both in terms of amplitude and phase profile), hence resulting in a perfect cloaking of the upstream scatterers. In other terms, the lack of impedance matching due to the presence of double-zero effective properties is balanced by the TA growth mechanism. Note that we did not show a numerical validation of these results because our model does not integrate nonlinear losses.

Interestingly, the same phase invariant behavior can be explored by homogenizing the TA waveguide so it behaves as an acoustic Willis material. The homogenization approach follows the discussion in Sec. III A. Dividing ω on both sides, Eq. (12) yields the expression of the effective refractive index:

$$n_{\text{eff}} = \tfrac{1}{2}[\eta_{\text{eff}} + \gamma_{\text{eff}} \pm \sqrt{(\eta_{\text{eff}} - \gamma_{\text{eff}})^2 + 4\rho_{\text{eff}}\beta_{\text{eff}}}]. \quad (19)$$

As a validation, we calculated the spatial phase distribution $\phi_p(x) = \arg(p(x))$ along a finite-length TA waveguide consisting of 40 unit cells in Fig. 11. In Figs. 11(a) and 11(b), the waveguide is excited at either the right or the left end (to excite either a forward- or backward-moving wave) with a zero phase ($\theta = 0$) at frequency $f = 17.15$ [Hz]. In each simulation, the end without excitation was terminated with an impedance matching boundary condition to eliminate unwanted reflections. See the Appendix for more details about numerical modeling. The specific frequency value was selected in a range that exhibits the phase-invariant transition phenomenon associated with the mode being excited. The calculations were conducted via two different approaches: (1) 2D numerical finite element simulations using COMSOL MULTIPHYSICS (blue solid curve) and (2) the effective model (red dashed curve), described in Eq. (19). The finite element solution was obtained to serve as a reference to validate the effective formulation. The effective formulation allowed calculating the spatial phase as $\phi_p(x) = \theta + \arg[\exp(-in_{\text{eff}}\omega(x - x_0))]$, where $\omega = 2\pi f$ is the angular frequency, x_0 is the point of application of the mechanical excitation [i.e., $x_0 = 40L$ for Fig. 11(a) and $x_0 = 0$ for Fig. 11(b)] and n_{eff} is the effective refractive index calcu-

lated based on the aforementioned homogenization approach [Eq. (19)]. We highlight that n_{eff} was calculated separately for the two counterpropagating modes [note the $\pm$ sign in Eq. (19)]. The comparison between Figs. 11(a) and 11(b) clearly captures the nonreciprocal behavior of the TA waveguide, which is shown by the asymmetric phase distribution under the two excitations. More importantly, the results from the two methods are in excellent agreement, hence confirming the validity of the homogenization approach based on a Willis material argument. We further note that the classical range of validity of homogenization, which states $L/\lambda \ll 1$ where λ is wavelength, is still applicable to the homogenization approach we adopted.

An additional interesting aspect of this class of 1D acoustic metamaterials consists of the ability to tune the refractive index by adjusting the intensity of the temperature gradient. Figure 8(e) shows that only the lower mode is capable of zero refractive index in the low-frequency range. Therefore, the tuning effect of the temperature gradient T_h/T_c is illustrated for this specific mode. Using the regular TA waveguide illustrated above, we performed a parametric study by varying the temperature ratio T_h/T_c. The numerical results presented in Fig. 12 show that as the temperature ratio increases, which is indicative of a more intense TA coupling, the refractive index Re[n] decreases. More remarkably, the effective zero range, that is, the range where Re[n] ≈ 0, is expanded as T_h/T_c increases. When $T_h/T_c = 3$, the refractive index is effectively zero in the reduced frequency range of approximately [0 ~ 0.02] where Re[n] is less than 1.5% of n_{ref} (Fig. 12 inset). n_{ref} is the refractive index of ambient air at T_c, that is, $n_{\text{ref}} = -1/a_0 = -2.915 \times 10^{-3}$[s/m]. Note that the negative sign corresponds to the negative intensity of the modes (blue) shown in Fig. 12. The range of [0 ~ 0.02] spans $\pm 100\%$ of the center (reduced) frequency, $(\omega_c L)/(2\pi a_0) = 0.01$, which is also indicative of the significant potential of TA waveguides to achieve broadband control. This latter characteristic also stems from the nonresonant nature of the present design. In Fig. 12, we included the effective refractive index calculated by Eq. (19) (diamonds) for the $T_h/T_c = 3$ case, which was extensively studied in Figs. 9–11. Again, excellent agreement is observed. For clarity, we do not show n_{eff} calculated from Eq. (19) for other T_h/T_c values.

Note that Re[n]/n_{ref} does not vanish at zero frequency. It is easily seen from the inset of Fig. 12 that Re[n]/n_{ref} crosses zero at a small but finite $\omega = \omega_0$ whose value depends on T_h/T_c, if $T_h/T_c \neq 1$. The frequency ω_0, which is not labeled explicitly in Fig. 12, indicates the intersection of the red horizontal axis (Re[n]/$n_{\text{ref}} = 0$) with each curve. If $\omega < \omega_0$, the effective medium is a negative index medium. Note that $n_{\text{ref}} = -1/a_0 < 0$, so Re[$n$]/$n_{\text{ref}} < 0$ denotes Re[n] > 0. Also note that the intensity has a negative sign (blue), that is, IRe[n] < 0, which is indicative of a negative index medium [55]. Nevertheless, ω_0 is typically very small but not quite zero. For practical considerations, we may consider the neighborhood of ω_0, including zero frequency, as the frequency range where the material is capable of zero refractive index or, equivalently, invariant phase transition. In the case of $T_h/T_c = 1$, the material does not exhibit a zero refractive index. Remember that $n \approx 0$ is induced by the significant TA coupling, which is represented by the term gu in Eq. (2). The
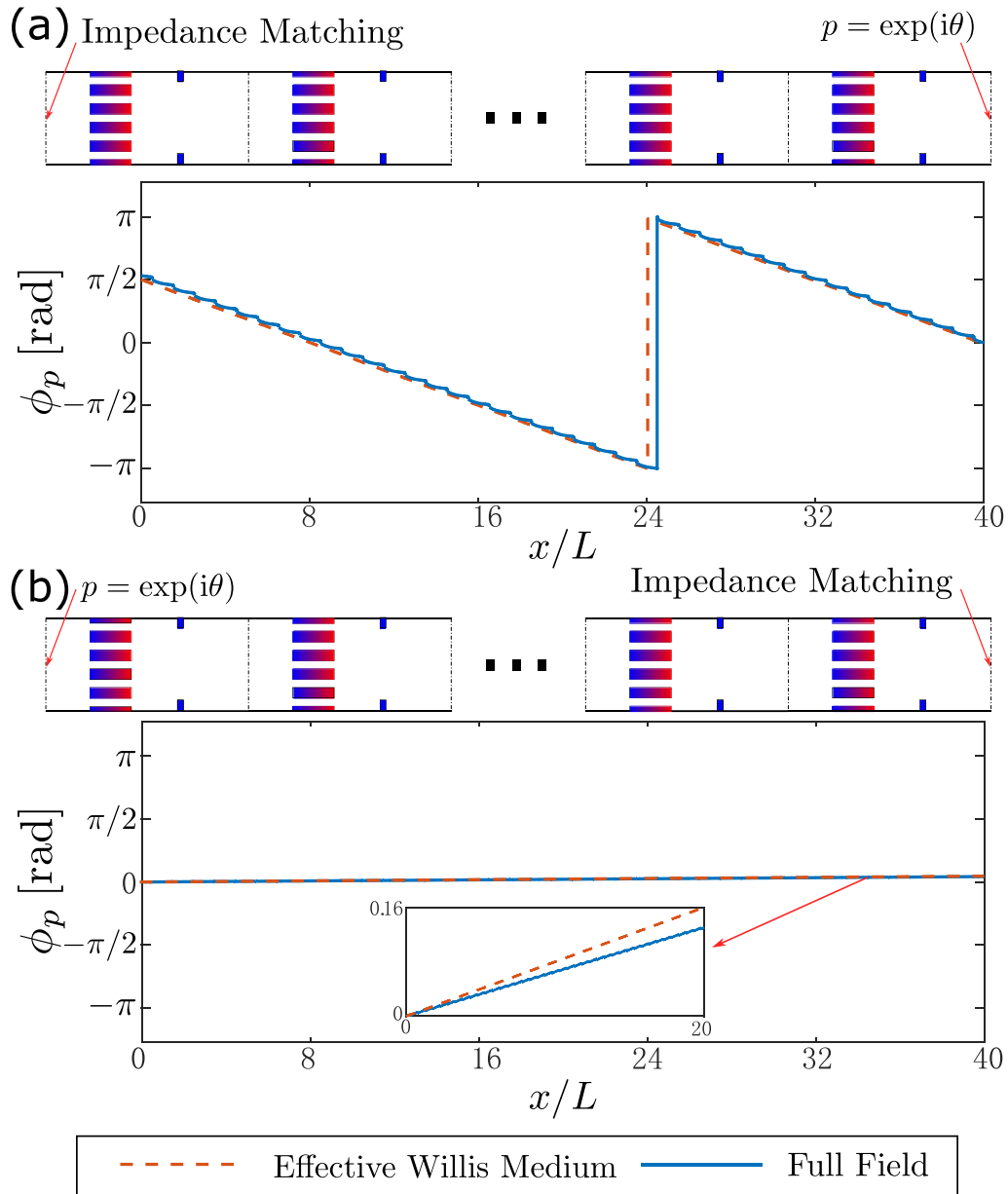
FIG. 11. The spatial phase distribution $\phi_p(x)$ along a finite-length TA waveguide consisting of 40 unit cells. The waveguide is excited either at the (a) right or (b) left end of the waveguide ito excite either a forward- or backward-moving wave. The phase plots are clearly different due to the already established nonreciprocal behavior of the waveguide. The asymmetric phase distribution (dashed line) is very well captured by the proposed effective Willis medium approach as shown by the excellent agreement with the 2D finite element simulation performed via COMSOL MULTIPHYSICS (solid line).

thermoacoustic coupling (gu) is especially significant in the low-frequency range [as explained earlier; see also Im[γ_{eff}] in Fig. 4(d)]. However, the gu term vanishes when $T_h/T_c = 1$ [Eq. (3)]. As a result, the deviation of n from n_{ref} can still be seen when $T_h/T_c = 1$ (due to nonzero $f_\square$), but no zero refractive index region exists (see Fig. 12). In the same figure, we show that the effect of the gu term on n appears even with a very mild temperature gradient, $T_h/T_c = 1.1$, but the effect is limited to a very small frequency range where n_{eff} is near zero (see inset). By increasing the frequency, n_{eff} quickly ramps up and reaches a constant value, $n_{\text{eff}}/n_{\text{ref}} \approx 1.05$.

D. Wave amplification and attenuation in small channels

It is widely accepted in thermoacoustics that, when a temperature gradient is established along a small channel (small-channel limit, such as those in a REG), the volumetric velocity is *proportionally* amplified (attenuated) if the direction of propagation occurs along (against) the positive (i.e., rising) temperature gradient direction [20,56]. This fact can be expressed by the relation $U_h/U_c = T_h/T_c$, where U and T are volumetric velocity and temperature, while the subscripts denote the hot and cold ends of the small channel. We anticipate that, thanks to the modeling approach presented in the previous sections, we will be able to make an important discovery
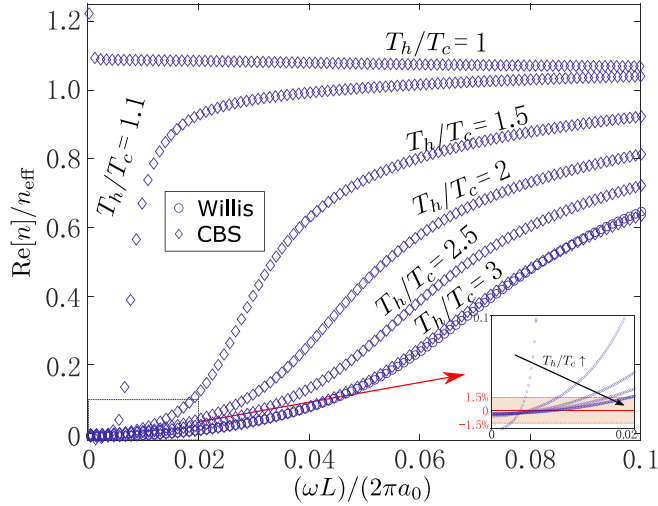
FIG. 12. Re[n] normalized by n_{ref}, as a function of the reduced frequency under different temperature gradients, T_h/T_c. $n_{ref} = -1/a_0$ is the refractive index of ambient air at $T_c = T_{ref} = 300$[K]. Results show that the refractive index of the TA waveguide and the bandwidth of the zero refractive index can be tuned by controlling the temperature ratio T_h/T_c. The effective refractive index calculated by the Willis medium dispersion relation [Eq. (12)] is also shown for the $T_h/T_c = 3$ case.

concerning the ideal limit behavior of the TA response. Indeed we will show that, unlike the conventional understanding of the small-channel limit behavior in classical thermoacoustics, the *proportional* relation ($U_h/U_c = T_h/T_c$) only holds for the spatially attenuating TA Bloch wave that propagates against the temperature rise. The proportional amplification along the temperature rise does not take place. This very important observation may have great implications for the optimal design of TA amplifiers [19].

Figure 3(b) shows that, as $\omega \to 0$, one branch of Im[k]L converges to a finite value, while the other branch converges to zero. This indicates that one mode propagates with an amplitude variation (Im[k]$L \neq 0$), while the other mode propagates with an unchanged amplitude (Im[k]$L = 0$). Whether the mode subject to amplitude variation undergoes spatial amplification or attenuation depends on the propagation direction of the mode. In the following, we theoretically prove that this limit behavior is always true and that the branch of Im[k]L converging to a finite value, proved to be Im[k]$L = \ln(T_h/T_c)$, is always associated with a negative intensity, indicative of a spatial attenuation.

As $\omega \to 0$, $h/2\delta_\square \to 0$, $f_v \to [1 - (2/3)(h/2)^2(\omega/2\nu)]$ under second-order approximation, hence, neglecting the higher order terms, Eqs. (1) and (2) can be recast into

$$\frac{dp}{dx} = -\frac{3\rho_0\nu}{(h/2)^2}u, \qquad (20)$$

$$\frac{du}{dx} = -\frac{i\omega}{P_m}p + \frac{dT_m}{T_m dx}u. \qquad (21)$$

Considering that the effect of the temperature gradient overpowers the viscous effect, Eq. (21) becomes

$$u_h = (T_h/T_c)u_c, \qquad (22)$$

where u_h and u_c are the cross-sectionally averaged particle velocities at the REG ends.

Two solutions are possible: (1) $u_h = u_c = 0$ and (2) $u_h/u_c = T_h/T_c$. Solution (1) is trivial and leads to a constant pressure p distribution according to Eq. (20) or, equivalently, Im[k]$L = 0$. Solution (2), under the long-wavelength assumption (small Re[k]L), leads to $u(L)/u(0) = u_h/u_c = T_h/T_c = \exp(\text{Im}[k]L)$. Therefore, Im[$k$]$L = \ln(T_h/T_c)$. This conclusion is also consistent with the classical understanding of TA waves in the small-channel limit ($h/2\delta_\square \to 0$) [56], which in Swift's words is stated as *"The volume flow rate is amplified in proportion to the temperature rise (or attenuated in proportion to a temperature drop)."* It is understood, based on the previous analysis, that as $\omega \to 0$ there can be only one wave type (either the forward- or backward-propagating wave) satisfying $u_h/u_c = T_h/T_c$.

In the following, we show that in the small-channel limit ($\omega \to 0$ or, equivalently, $h/2\delta_\square \to 0$) only the ideal proportional attenuation along the temperature drop (associated with a negative intensity or, equivalently, backward-propagating wave) is possible.

For the mode satisfying $u_h/u_c = T_h/T_c$, the velocity distribution in the REG is proportional to $T_0(x)$, i.e.,

$$u(\xi) = C[a\xi + T_c], \qquad (23)$$

where $\xi = x - x_c$, $a = (T_h - T_c)/(x_h - x_c)$, and C is an arbitrary proportional constant. According to Eq. (20), the pressure p in the REG is expressed as

$$p(\xi) = -\frac{3\rho_0\nu}{(h/2)^2}C\left[\frac{1}{2}a\xi^2 + T_c\xi + \frac{(T_h + T_c)Tc}{2a}\right]. \qquad (24)$$

Therefore, the intensity at the cold end of the REG ($\xi = 0$) is

$$I = \frac{1}{2}\text{Re}[p\bar{u}] = -\frac{1}{2}\frac{3\rho_0\nu}{(h/2)^2}|C|^2\frac{(T_h + T_c)T_c^2}{2a} < 0. \qquad (25)$$

Note that, in the case of TA amplifiers, it is always desirable to achieve the maximum amplification factor, which according to classical thermoacoustics is $u_{out}/u_{in} = u_h/u_c = T_h/T_c$ for a single TA unit [20,56]. Based on the conventional understanding [20,56], this theoretical extreme can be achieved in the small-channel limit. However, the previous TA Bloch wave analysis shows that such ideal change of u proportional to the temperature gradient is always accompanied by a negative intensity I (indicating a spatial attenuation of the wave along $-x$). Nevertheless, by careful design, one can still get close to (although never reach) the ideal amplification of u along the temperature rise. Figure 13 shows the imaginary part of the CBS of a TA Bloch wave in the low-frequency range obtained with another set of parameters: $x_1 = 0.1$, $x_2 = 0.13$, $x_3 = 0.16$, $h_s = 0.96$[mm] $= 5.714h$. Note that the ratio $h_s/h = 5.714 > 1$ represents a locally enlarged REG. The parameters were modified with respect to the analysis in Fig. 3 because, according to Ceperley [56] and Senga and Hasegawa [19], the higher impedance induced by an enlarged REG improves the TA energy conversion efficiency, which is beneficial to the wave amplification in the low-frequency range. It can be seen that, although the right branch emanating from Im[k]L=ln(1.5)=0.405 has negative intensity (blue) as $\omega \to 0$, the intensity soon becomes positive (yellow) with
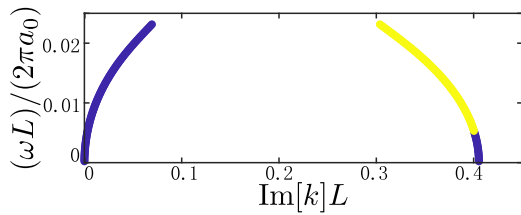
FIG. 13. Imaginary part of the CBS for the waveguide in TA configuration under a prescribed set of parameters (see the text). Results show that the ideal amplification of u along the direction of the temperature rise (yellow-colored solution with the value of $\mathrm{Im}[k]L = \ln[T_h/T_c] = 0.405$ as $\omega \to 0$) can be closely approached but never reached.

increasing ω. In other terms, a forward-moving Bloch wave, denoted by a positive intensity, is spatially amplified with a rate that reaches the maximum theoretical amplification rate $\mathrm{Im}[k]L \approx \ln(T_h/T_c)$. However, as $\omega \to 0$, the intensity associated with both modes become negative (denoted by blue curves in Fig. 13), which is a sign of unidirectional energy transport. This aspect has been discussed in detail in Sec. III B.

This underlying behavior in the small-channel limit was not observed before and it might have substantial implications to guide the optimal design of TA diodes and amplifiers.

IV. CONCLUSIONS

This paper presented an in-depth theoretical and numerical investigation of the dispersion and propagation characteristics of Bloch waves occurring in an acoustic periodic waveguide in the presence of TA coupling. This class of waves was dubbed TA Bloch waves. The work highlighted several noteworthy findings concerning the basic physical behavior of this wave type as well as their potential impact on future applications. While the static temperature gradient imposed on each REG led, as expected, to breaking the intrinsic reciprocity of the waveguide, we provided an in-depth interpretation of the TA nonreciprocity by showing that the TA waveguide can be seen as an acoustic Willis medium. The TA Bloch wave also highlighted several other very intriguing and unexpected propagation phenomena. Indeed, by leveraging a complex band-structure approach, we uncovered an anomalous unidirectional energy transport unique to this type of waveguide. The energy transport was also found to be significantly different depending on the nature of the acoustic wave, that is, a wave packet or a harmonic wave, potentially resulting in contrasting directions for the transfer of macroscopic and microscopic energy.

Also remarkable was the ability of the TA waveguide to act as a broadband, tunable, effective zero refractive index material. In selected frequency ranges, the waveguide was shown to achieve zero effective refractive index. In addition, the refractive index could be tuned by simply controlling the intensity of the temperature gradient. The zero-index nature of the TA waveguide was shown to enable phase invariance of the pressure field within the TA waveguide, hence showing potential for application of efficient energy transmission and acoustic cloaking devices. Also very remarkable was the improved understanding of the TA amplification and attenuation

effects in the small-channel limit. Specifically, the finding that the amplifying mode can never achieve the theoretical limit could have a significant impact on the optimal design of TA diodes or amplifiers.

APPENDIX: ADDITIONAL REMARKS ON NUMERICAL SIMULATIONS

In this paper, we adopted two main models: (1) a quasi-1D analytical model used to formulate an eigenvalue problem [Eq. (8)] solved via finite difference method and (2) a finite element model implemented via the commercial software COMSOL Multiphyscis.

The first model was presented in Sec. II, including the key steps that eventually led to a generalized eigenvalue problem, Eq. (8). The formulation of Eq. (8) was established based on the discretization of the governing equations, including Eqs. (1) and (2) that govern the TA waves in the REG channels, and the Helmholtz equation that governs the plane waves outside of the REG. The unit cell was discretized so p and u were arranged on a staggered grid to apply central finite differences; a commonly used numerical treatment in thermoacoustics (see, for example, Fig. 3 in Ref. [31]). Note that the frequency ω is absorbed in the two coefficient matrices **A** and **B**. Clearly, when ω is entered as a known parameter, the eigenvalue problem has the eigenvalue $\exp(-ikL)$ and the eigenfunction $[\mathbf{p}, \mathbf{u}]^{\mathrm{T}}$. Knowing both **A** and **B**, Eq. (8) can be solved with any commercially available eigenvalue package, such as that in MATLAB. With any input ω, the solution includes two eigenvalues or, equivalently two k's, and two eigenfunctions $[\mathbf{p}, \mathbf{u}]^{\mathrm{T}}$. This approach allowed us to calculate the CBS (Figs. 2 and 3), as well as the effective Willis properties (Fig. 11) using the eigenfunctions.

In the finite element models, the geometry of a TA waveguide was created first. The geometry of a unit cell is depicted in Fig. 1(a) (bottom). In each unit cell, the fluid channel within REG is surrounded by walls on which nonslip, isothermal boundary conditions are assigned to capture the diffusion process (of temperature and velocity) in the transverse direction. Other walls are assigned slip, adiabatic boundary conditions to impose the lossless plane-wave assumption. At the two ends of a finite waveguide, different boundary conditions are applied. For example, in the time-dependent transient analysis shown in Fig. 5, the boundary conditions at both ends of the waveguide are irrelevant since we halted the simulation before the waves were reflected by the boundaries. However, in the frequency-dependent steady-state analyses (Figs. 9–11), we applied a harmonic pressure excitation on either side of the finite-length waveguide, depending on the target mode we intended to excite. On the nonexcitation side, an impedance matching boundary conditions was applied. The impedance matching boundary condition was set up by assigning a value as the normal impedance of the boundary to the termination of the computational domain. This value can be either extracted from our theoretical modeling using $z = p/u$, where both p and u are available from Eq. (8), or from the iterative evaluation of the impedance at the interface of two in-domain unit cells. Note that for an infinite periodic waveguide, the impedance at any interface of two connecting cells should be identical. Therefore, to effectively truncate the computational

domain for a finite periodic waveguide, this impedance value was also assigned to the boundary. The static temperature profile [Fig. 1(b)] was assigned as a base (zeroth order) temperature in COMSOL, which (1) defines the distribution of the temperature-dependent material properties (sound speed and viscosity) along the waveguide and (2) activates the convective derivative $\mathbf{u} \cdot \nabla T_0$ in the heat equation, where $\mathbf{u}$

is the particle velocity vector and ∇ denotes gradient. This convective term, which eventually leads to the *gu* term upon 1D simplification [29], is the key contributor to almost all anomalous phenomena connected to the TA coupling. Finally, but not less important, the mesh in the REG channels was refined so the transverse diffusion, which is crucial to TA coupling, was effectively resolved.

[1] R. Fleury, D. L. Sounas, C. F. Sieck, M. R. Haberman, and A. Alù, Science **343**, 516 (2014).

[2] R. Fleury, D. L. Sounas, and A. Alù, Phys. Rev. B **91**, 174306 (2015).

[3] N. Swinteck, S. Matsuo, K. Runge, J. O. Vasseur, P. Lucas, and P. A. Deymier, J. Appl. Phys. **118**, 063103 (2015).

[4] N. Boechler, G. Theocharis, and C. Daraio, Nature. Mater. **10**, 665 (2011).

[5] B. Liang, B. Yuan, and J.-c. Cheng, Phys. Rev. Lett. **103**, 104301 (2009).

[6] B. Liang, X. S. Guo, J. Tu, D. Zhang, and J. C. Cheng, Nature. Mater. **9**, 989 (2010).

[7] S. Zhu, T. Dreyer, M. Liebler, R. Riedlinger, G. M. Preminger, and P. Zhong, Ultrasound Med. Biol. **30**, 675 (2004).

[8] S. Barzanjeh, M. Wulf, M. Peruzzo, M. Kalaee, P. B. Dieterle, O. Painter, and J. M. Fink, Nat. Commun. **8**, 953 (2017).

[9] Z. Yang, F. Gao, X. Shi, X. Lin, Z. Gao, Y. Chong, and B. Zhang, Topological Acoustics, Phys. Rev. Lett. **114**, 114301 (2015).

[10] X. Ni, C. He, X.-C. Sun, X.-P. Liu, M.-H. Lu, L. Feng, and Y.-F. Chen, New J. Phys. **17**, 053016 (2015).

[11] T.-W. Liu and F. Semperlotti, Phys. Rev. Appl. **9**, 014001 (2018).

[12] T.-W. Liu and F. Semperlotti, Adv. Mat. **33**, 2005160 (2021).

[13] Y. Li, B. Liang, Z.-m. Gu, X.-y. Zou, and J.-c. Cheng, Appl. Phys. Lett. **103**, 053505 (2013).

[14] T. Yazaki, A. Iwata, T. Maekawa, and A. Tominaga, Phys. Rev. Lett. **81**, 3128 (1998).

[15] G. Swift, J. Acoust. Soc. Am. **84**, 1145 (1988).

[16] P. Gupta, G. Lodato, and C. Scalo, J. Fluid. Mech. **831**, 358 (2017).

[17] H. Hao, C. Scalo, and F. Semperlotti, J. Sound. Vib. **449**, 30 (2019).

[18] T. Biwa, H. Nakamura, and H. Hyodo, Phys. Rev. Appl. **5**, 064012 (2016).

[19] M. Senga and S. Hasegawa, J. Appl. Phys. **119**, 204906 (2016).

[20] G. W. Swift, *Thermoacoustics A Unifying Perspective for Some Engines and Refrigerators*, 2nd ed. (Springer, Cham, Switzerland, 2017).

[21] C. Scalo, S. Lele, and L. Hesselink, J. Fluid. Mech. **766**, 368 (2015).

[22] G. Chen, L. Tang, and B. Mace, Int. J. Heat Mass Transf. **123**, 367 (2018).

[23] H. Hao, C. Scalo, M. Sen, and F. Semperlotti, J. Appl. Phys. **123**, 024903 (2018).

[24] Y.-F. Wang, Y.-S. Wang, and V. Laude, Phys. Rev. B **92**, 104110 (2015).

[25] Y. Liu, D. Yu, H. Zhao, J. Wen, and X. Wen, J. Phys. D Appl. Phys. **41**, 065503 (2008).

[26] J. Hwan Oh, Y. Jae Kim, and Y. Young Kim, J. Appl. Phys. **113**, 106101 (2013).

[27] G. Theocharis, O. Richoux, V. R. García, A. Merkel, and V. Tournat, New J. Phys. **16**, 093017 (2014).

[28] V. C. Henríquez, V. M. García-Chocano, and J. Sánchez-Dehesa, Phys. Rev. Appl. **8**, 014029 (2017).

[29] N. Rott, Z. Angew. Math. Phys. **20**, 230 (1969).

[30] M. Guedra and G. Penelet, Acta. Acust. united Ac. **98**, 232 (2012).

[31] J. Lin, C. Scalo, and L. Hesselink, J. Fluid. Mech. **808**, 19 (2016).

[32] G. Chen, L. Tang, and B. R. Mace, Appl. Therm. Eng. **150**, 532 (2019).

[33] H. Hao, C. Scalo, and F. Semperlotti, J. Sound. Vib. **470**, 115159 (2020).

[34] H. Hao, C. Scalo, and F. Semperlotti, Mech. Syst. Signal. Process. **148**, 107143 (2021).

[35] T. Suzuki and P. K. Yu, J. Mech. Phys. Solids **46**, 115 (1998).

[36] S. Cummer, J. Christensen, and A. Alù, Nat. Rev. Mater. **1**, 16001 (2016).

[37] G. Chen, L. Tang, B. Mace, and Z. Yu, Renew. Sustain. Energy Rev. **146**, 111170 (2021).

[38] H. Nassar, B. Yousefzadeh, R. Fleury, M. Ruzzene, A. Alú, C. Daraio, A. N. Norris, G. Huang, and M. R. Haberman, Nat. Rev. Mater. **5**, 667 (2020).

[39] M. B. Muhlestein, C. F. Sieck, A. Alú, and M. R. Haberman, Proc. R. Soc. A **472**, 20160604 (2016).

[40] L. Quan, D. L. Sounas, and A. Alù, Phys. Rev. Lett. **123**, 064301 (2019).

[41] C. Kittel, Phys. Rev. **110**, 836 (1958).

[42] S. Nemat-Nasser and A. Srivastava, J. Mech. Phys. Solids **59**, 1953 (2011).

[43] A. Srivastava and S. Nemat-Nasser, Proc. R. Soc. A **468**, 269 (2012).

[44] A. N. Norris, A. L. Shuvalov, and A. A. Kutsenko, Proc. R. Soc. A **468**, 1629 (2012).

[45] M. B. Muhlestein, C. F. Sieck, P. S. Wilson, and M. R. Haberman, Nat. Commun. **8**, 15625 (2017).

[46] J. Tan, J. Wei, and T. Jin, Appl. Energy **262**, 114539 (2020).

[47] C. Shi, M. Dubois, Y. Wang, and X. Zhang, Proc. Natl. Acad. Sci. **114**, 7250 (2017).

[48] C. E. Bradley, Linear and nonlinear acoustic Bloch wave propagation in periodic waveguides, Technical Report No. ARL-TR-94-10, The University of Texas at Austin, 1994.

[49] T. Jin, R. Yang, Y. Wang, Y. Liu, and Y. Feng, Appl. Energy **183**, 290 (2016).

[50] K. Luo, J. Hu, E. Luo, L. Zhang, Y. Sun, and Y. Zhou, Cryogenics **98**, 5 (2019).

[51] M. Dubois, C. Shi, X. Zhu, Y. Wang, and X. Zhang, Nat. Commun. **8**, 14871 (2017).

[52] X.-F. Zhu, Phys. Lett. A **377**, 1784 (2013).

[53] H. Zhu and F. Semperlotti, Phys. Rev. Appl. **8**, 064031 (2017).

[54] N. Kaina, F. Lemoult, M. Fink, and G. Lerosey, Nature (London) **525**, 77 (2015).

[55] T. A. Klar, A. V. Kildishev, V. P. Drachev, and V. M. Shalaev, IEEE J. Sel. Top. Quantum Electron **12**, 1106 (2006).

[56] P. Ceperley, J. Acoust. Soc. Am. **66**, 1508 (1979).